






Polarization-dependent wideband metamaterial absorber for ultraviolet to near-infrared spectral range applications

FANGFANG LI,¹ IBRAHIM ISSAH,^{2,4}  MARIAN BAAH,¹ REUBEN AMEDALOR,¹ MIRIAM QUARSHIE,¹ PRINCE BAWUAH,^{1,3}  AND BENJAMIN O. ASAMOAH^{1,5} 

¹*Department of Mathematics and Physics, University of Eastern Finland, P.O. Box 111, FI-80101 Joensuu, Finland*

²*Faculty of Engineering and Natural Science, Photonics, Tampere University, 33720 Tampere, Finland*

³*Department of Chemical Engineering and Biotechnology, University of Cambridge, Philippa Fawcett Drive, Cambridge CB3 0AS, UK*

⁴*ibrahim.issah@tuni.fi*

⁵*benjamin.asamoah@uef.fi*

Abstract: The need for wideband metamaterial absorbers (WBMA) for applications other than sensing and filtering has demanded modifications to the conventional three-layer metal-insulator-metal (MIM) absorber configuration. This modification often results in complex geometries and an increased number of layers requiring complex lithographic processes for fabrication. Here, we show that a metamaterial absorber with rectangular geometry in the simple MIM configuration can provide wideband absorption covering the ultraviolet and near-infrared spectral range. Due to its asymmetric nature, the WBMA is sensitive to the polarization of the incident light and independent of the angle of incidence up to about 45° depending on the polarization of the incident light. The characteristics of the WBMA presented here may be useful for applications such as detectors for wide spectral band applications.

© 2022 Optica Publishing Group under the terms of the [Optica Open Access Publishing Agreement](#)

1. Introduction

The ability to control light interaction with matter is very desirable in many applications such as selective filtering, solar absorption, light extraction, sensing, etc [1–4]. Since natural materials are limited in their functionalities, in this regard, metamaterials with engineered functionalities that can be tailored for specific applications have been the focus of many researchers. This popularity is in part associated with the advancement of fabrication techniques that allows the possibility to fabricate subwavelength structures [5,6] and mostly the well-developed understanding of plasmonic techniques in metal-related applications [7]. In particular, metamaterial absorbers capable of achieving high absorption is popular among engineered materials [8]. However, the absorption capabilities of these metamaterials are usually limited to a finite spectral range making them suitable for narrowband filtering and sensing applications, [1–3], for example, as this type of absorbers typically support either Fabry-Perot mode, localized surface plasmon modes or both [9–11].

For certain applications such as thermal management, wide-spectrum photodetectors, and photovoltaics for energy harvesting and heating [4,12,13] that require a broad spectral operating range, the use of narrow-band metamaterials become limited. Given the desire to achieve broadband metamaterial absorbers, the use of different techniques, among which is the exploitation of different geometries, has been one of the most popular approaches. A straightforward approach is to exploit different geometries with narrow absorbance at different wavelengths in a unit cell [14]. For example, whilst a unit cell with a square symmetry of Aluminium (Al) nanodisks,

achieves relatively narrow absorption bands [15], a unit cell with hexagonal symmetry of similar Al nanodisks has been exploited to obtain absorbance in the visible (Vis)-near-infrared (NIR) spectral range [16]. Alternatively, in the usual three-layer metal-insulator-metal (MIM), different geometric structures have also been exploited. In [17], Wang et al. have used a T-shaped polymer encapsulated with a thin layer of chromium (Cr) to achieve wide absorbance in the Vis-NIR range. Similarly, an ultrabroad absorbance for a four-headed arrow-shaped titanium (Ti) structure has also been demonstrated in [18]. Yet another approach, as demonstrated in [19], is by capping some simple geometrical structures such as nanodisks and squares. Similarly, by using truncated pyramids, high broadband spectral absorbance spanning 400 – 1100 nm has been achieved by Dang et al., [20].

Lastly, by simply increasing the number of layers for the metamaterial absorber beyond the typical metal-insulator-metal (MIM) configuration for metamaterials absorbers, wider spectral absorbance has also been demonstrated. Using stacked metallic-dielectric layers where the number of layers corresponds to the number of observed peaks, a total of seven absorption peaks were obtained in the Vis-NIR spectral range [11]. Adding to the above examples, a four-layer structure (SiO₂-Ti-MgF₂-Al) [21] has been studied numerically. Also, a six-layer absorber [22] as well as a truncated square-based pyramid consisting of 20 layers of Au-Ge for plasmon hybridization [23] have been used to obtain ultrabroad absorption. The complexity of the metamaterial structures seems to correlate with the broad absorption. Recently, Zhou, et al. have demonstrated ultra-broadband absorption in the long infrared regime using four layers of either Ti-Ge-Si₃N₄-Ti or Ti-Ge-SiO₂-Ti [24].

Undoubtedly, while these innovative structures have been particularly useful in achieving wider spectral absorbance, they have also placed a huge demand on fabricating them due to the complexity and increase in the number of layers. It seems not surprising, therefore, that most of these complex structures are only studied numerically. Moreover, for absorbers operating in the Vis-NIR spectral range, in particular, the absorption bandwidth for these structures is typically a little over 1000 nm [10,25].

In this study, we show that a simple MIM consisting of Ti-SiO₂-Ti is still competitive in achieving wide-band absorption for applications in the Ultraviolet to near-infrared (UV-NIR) spectral range, 250 – 1600 nm. Here, we show that by using such a simple rectangular geometrical structure as a top layer, an average absorption greater than 90% can be achieved at normal incidence illumination for certain polarization. We also calculated the field distribution at suitable absorption wavelengths to determine the origin of the observed resonance in the wideband metamaterial absorber (WBMA). Further, we performed different parametric sweeps to determine the effect of structural parameters on the spectral absorbance of the WBMA. Although the proposed absorber exhibits significant polarization sensitivity in the NIR range, it is insensitive for angles of incidence up to about 45 °.

2. Materials and methods

2.1. Structure design and modelling

The proposed WBMA comprises Ti-SiO₂-Ti layers with a rectangular unit cell stacked on top of the SiO₂ spacer and Ti films as illustrated in Fig. 1. The wavelength-dependent complex refractive index of Ti and SiO₂ were obtained from ellipsometric measurement, see Fig. S1. The choice of Ti is to exploit its lossy properties in the NIR for increased absorbance [24–26]. The absorbance, electromagnetic field distributions, and current density were calculated using the Finite-Difference Time-Domain (FDTD) method. The simulation region dimension was set to a 3-D layout with a period of 250 nm in both x- and y-directions, and a perfectly matched layer (PML) boundary condition set in the z-direction. We utilized the symmetric boundary conditions, conformal variant mesh, and increased the simulation time to ensure that the electromagnetic field sufficiently decays.

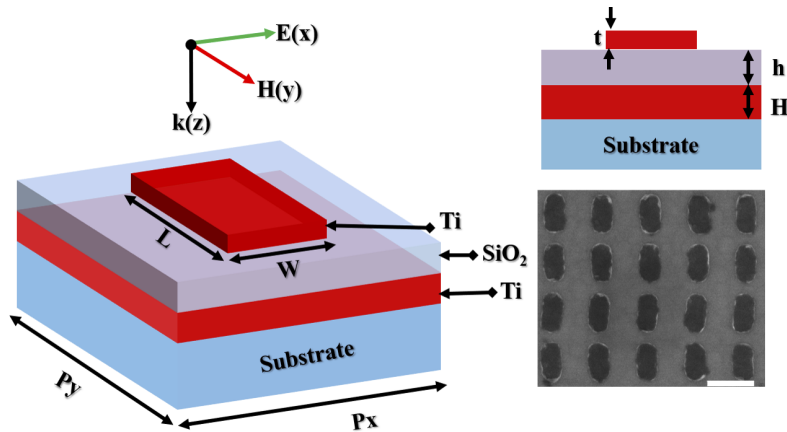


Fig. 1. Schematics of the wideband metamaterial absorber. The inset show the SEM image of the fabricated structure. The black dash line correspond to the 250 nm.

A plane wave, propagating normal to the interface, at different polarization angles was used as the incident source to calculate the absorbance using a spectral-domain field monitor. Similar calculations were also carried out at selected oblique incidence. The numerically simulated absorbance spectra show a good match with the experimental results for the following parameters: bottom Ti-film thickness ($H = 100$ nm), SiO_2 -spacer thickness ($t = 100$ nm), thickness of the rectangular nanopatterned top-layer ($h = 45$ nm), rectangular width ($W = 100$ nm), and Length ($L = 200$ nm). A relatively thicker Ti-film at the bottom of the WBMA was chosen to decrease the transmittance such that the absorbance of the proposed structure can be approximated as $A = 1 - R$, where A is the absorbance and R is the reflectance spectra. The results also show polarization dependence in the spectral absorbance of the WBMA in the region of interest due to the asymmetric nature of the top rectangular structure. We examine the polarization dependence in all cases of the presented results, therefore.

2.2. Fabrication and characterization

The WBMA absorber was fabricated on fused silica substrates. The substrates were cleaned following the usual cleaning procedure namely acetone and isopropanol in an ultrasonic bath followed by cleaning with de-ionized water and oxygen plasma. Following the cleaning, 100 nm-thick of titanium (Ti) was sputtered on the substrate using (Quorum Technologies Ltd, Q300TT plus, United Kingdom) to form the bottom layer. On top of the Ti-film, another 100 nm-thick layer of silicon dioxide (SiO_2) was thermally deposited at 300°C using atomic layer deposition (ALD, TFS 200, Beneq Oy, Finland) as the dielectric layer. The final layer was patterned using lithographic techniques. Positive polymethylmethacrylate (PMMA) resist was spin-coated at 3000 rpm for 60 s and post-baked for 5 mins at 150°C to obtain 300 nm-thick layer. After thermally depositing a 30 nm-thick copper (Cu) film as a conductive layer, the resist was exposed using electron-beam lithography (EBPG5000+ES HR, Vistec Lithography, Netherlands). The exposed samples were then developed in a medium contrast developer, Methyl Isobutyl Ketone MIBK: Isopropyl Alcohol IPA (1:2), after the removal of the conductive layer. Finally, 45 nm-thick Ti was then sputtered, and the unpatterned resist removed by the lift-off process. The scanning electron micrograph of the fabricated sample is shown as an inset in Fig. 1.

To characterize the spectral absorbance of the structures, two types of spectrophotometers were used namely (Lambda 1050, Perkin Elmer, USA), with a wider spectral range, and a spectrometer

(Ocean Insight, USA). All experimental measurements were carried out for normal incidence using an unpolarized excitation source.

3. Results and discussion

3.1. Spectral response

Figure 2 shows the spectral absorbance of the wideband metamaterial absorber (WBMA) in the UV-NIR spectral range for normal incidence. Two absorption peaks can be immediately identified; one with near-perfect absorption at 280 nm and another broadband at ~ 1025 nm for both simulation (green dash line) and experiment (black solid line) for the unpolarized case. While the band for the near-perfect absorption in the UV spectral is broader for the experimental results, the similarity between the simulation and experiment for the broadband is remarkable. The difference between experiment and simulation for the near-perfect absorption at 280 nm could arise from the imperfections in the fabricated structure, as seen in Fig. 1, that leads to the inhomogeneous broadening of the band. Due to the asymmetry of the top rectangular structure, we also simulated the polarization dependence of the absorption of the WBMA as can also be seen in Fig. 2.

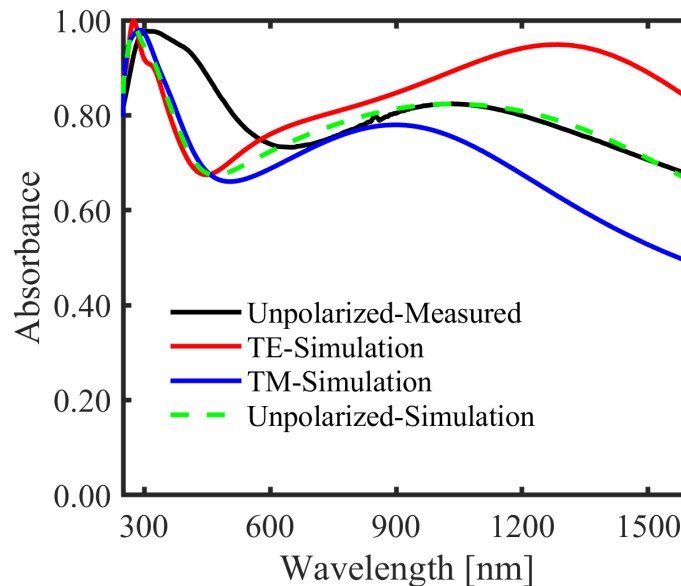


Fig. 2. Measured and simulated spectral absorbance of the WBMA in the Vis-NIR spectral range.

Indeed, the WBMA exhibits different responses for the two polarizations namely transverse electric (TE) and transverse magnetic (TM). While they both have similar near-perfect absorption at 280 nm, as the incident light sees the same periodicity in both orthogonal directions, the positions of the maximum peak in the broadband in the NIR spectral range are at different wavelengths due to the asymmetric geometry of the absorber. These locations are at ~ 1315 nm and ~ 911 nm for TE and TM, respectively.

For comparison, similar calculations and measurements were performed for the structure without the dielectric layer. The results are illustrated in Fig. S2. The experimentally measured spectral absorbance for the case of unpolarized light decreases monotonically, from $\sim 85\%$ to $\sim 70\%$, which agrees with the simulated results. In such a configuration, without the dielectric layer, the controlling mode is usually dominated by the localized surface plasmons [27] as the

incident light gets confined by the top nanostructure. Note that, in Fig. S2, both the TE and TM show little difference in the magnitude of the absorbance over the wavelength range, and that, when compared with the optimized case, the dielectric layer plays an important role in trapping and absorbing the resonant modes that contribute to the additional increase in absorption in the WBMA [24]. This is possible as the dielectric controls the phase accumulation of the transmitted and reflected light to and from the bottom Ti film. Minimum reflection occurs when there is constructive interference [28] of light from its top and bottom interfaces. The decrease in the overall absorption in Fig. S2 can, therefore, be attributed to its absence.

To further identify the resonances in the absorption spectrum, the electromagnetic fields were simulated and analyzed. Overall, the two resonances for both polarizations exhibit different electric field distributions in the $x - y$ plane, as seen in Fig. S3. While the resonances in the UV exhibit a quadrupolar nature, with the field localized at the corners, the resonances in the NIR, on the other hand, show dipolar distribution. Figure 3 show the calculated electric (first column), magnetic (second column) field distributions and the current densities for the identified resonances in the vertical plane ($x - z$ or $y - z$) for the two polarizations. For the TE, at 280 nm, the electric field in Fig. 3(a), is strongly confined around the four edges of the top rectangle as well as above it. The high charge distribution that typically exists at sharp edges leads to the so-called lightning-rod effect due to the higher-order modes [18]. Similarly, there exists an electric field within the dielectric layer extending to neighbouring unit cells with increased intensity moving away from below the edges of the rectangle. This behavior in addition to the parallel vector field lines as seen in Fig. S3 (a) in the $x - y$ plane is consistent with surface plasmons polaritons (SPP) that exist between the bottom Ti film and the dielectric layer. The corresponding magnetic field distribution illustrated in Fig. 3(b), on the other hand, exhibit different modes. In addition to the enhanced field on the top of the structure, the magnetic field exhibits a cavity-mode-like behavior within the dielectric layer and higher-order propagating surface plasmons at the interface between the dielectric and the bottom Ti film [18,24].

For the resonance in the NIR at 1315 nm, the electric field is mainly enhanced between the unit cells of the top rectangular structure. The magnetic field is, however, strongly enhanced beneath the top layer and the bottom Ti film, gradually extending to the adjacent unit cells. Coupled with the distribution in Fig. S3 (b) of Supplement 1, these observations are attributed to the excitation of fundamental localized surface plasmon (LSP).

The resonances for the TM polarizations namely at 280 nm and 911 nm also exhibit similar field distributions as the TE with minor variations. In Fig. 3(h), the so-called cavity mode [18], in Fig. 3(b), is absent for the 280 nm. Moreover, unlike in the TE case, a fundamental PSP is excited rather than the higher-order mode, which modulates the cavity mode. The current density plots for the various modes in both polarizations, in the last column of Fig. 3, indicate the concentration of charges within the metals, which confirms that most of the identified resonances are indeed based on surface plasmons [19].

3.2. Impedance

The goal of metamaterials absorbers is to achieve maximum absorption in the spectral range of interest. In a typical MIM absorber, this means that the reflection of the incident light through the MIM structure is as minimum as possible whilst at the same time decreasing the transmission through the bottom layer. The former requires that the effective free space impedance (Z_0) is matched to that of the absorber (Z) to decrease the reflection from the structure. Theoretically, the effective impedance of the structure can be expressed in terms of the scattering (S -) parameters of the structures as,

$$Z = \pm \sqrt{\frac{(1 + S_{11})^2 - S_{21}^2}{(1 - S_{11})^2 - S_{21}^2}}, \quad (1)$$

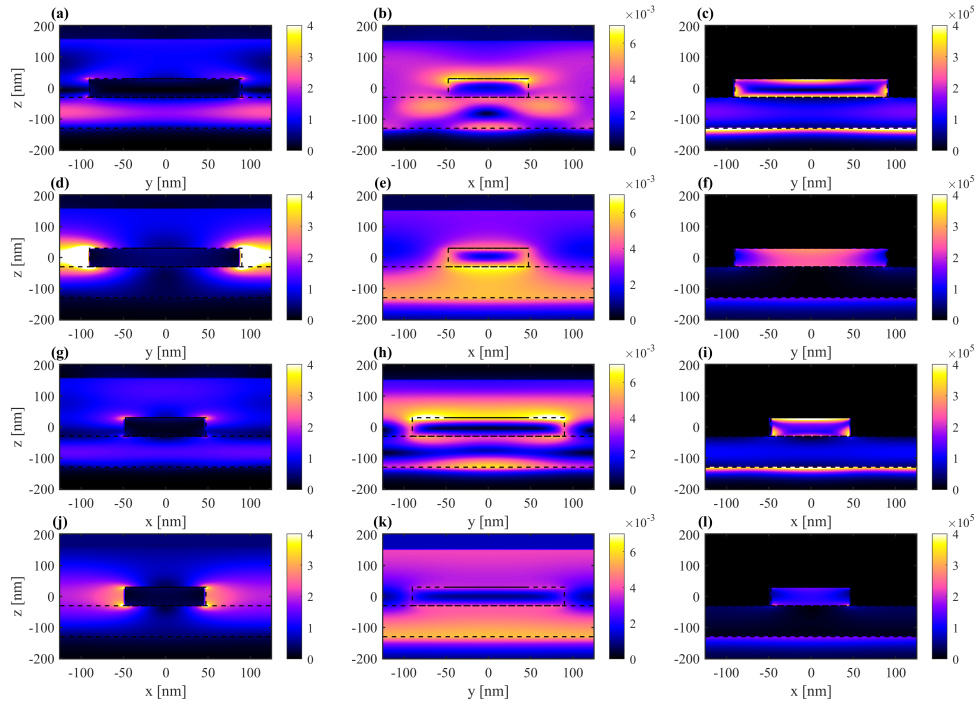


Fig. 3. Electric (first column), magnetic (middle column) field distributions, and current density (last column) calculated at 280 nm (a - c) and 1315 nm (d - f) for TE. Similar calculations for TM at 280 nm (g - i) and 911 nm (j - l).

where the S -parameters can be defined as [29] in Eqs. (2) and (3)

$$S_{21} = S_{12} = \frac{1}{\cos(nkd) - \frac{i}{2} \left(Z + \frac{1}{Z} \right) \sin(nkd)}, \quad (2)$$

$$S_{11} = S_{22} = \frac{i}{2} \left(\frac{1}{Z} - Z \right) \sin(nkd) \quad (3)$$

and S_{21} , S_{12} , S_{11} , S_{22} are the S -parameters, whereas n , k , and d are the effective refractive index, the propagation constant (wave vector), and thickness of the structure, respectively. S_{21} is the forward transmission, S_{12} is the backward transmission, S_{11} is the forward reflection, and S_{22} is the backward reflection. By setting the thickness of the bottom layer greater than the skin depth of the impinging wavelength, the transmission goes to zero i.e. $S_{21} = 0$ and Eq. (1) then reduces to

$$Z = \pm \left(\frac{1 + S_{11}}{1 - S_{11}} \right). \quad (4)$$

The reflectance of the optimized structure can then be expressed in terms of the free space and absorber impedance in Eq. (5)

$$R = \left[\frac{Z - Z_0}{Z + Z_0} \right]^2. \quad (5)$$

Obviously, with $Z = Z_0$, the reflectance goes to zero and maximum absorption of unity can be obtained as the transmission is also zero. Since the effective impedance can equally be expressed as $Z(\lambda) = \sqrt{\frac{\mu(\lambda)}{\varepsilon(\lambda)}}$; where $\mu(\lambda)$ and $\varepsilon(\lambda)$ are the effective permeability and permittivity of the

structure, the consequence of the unity absorption in metamaterial absorber is that the electric and magnetic resonance must be equal. And by manipulating the scattering properties, this can be achieved.

Figure 4 shows the calculated values for S_{11} and S_{21} parameters (a) and their corresponding phases (b) of the propagating incident light, and the overall impedance of the structure (c) for TE and TM polarizations. Evidently, S_{21} is close to 0 for both polarizations as predicted in Eq. (4) indicating that the bottom Ti layer acts as a mirror for the proposed structure. On the contrary, the S_{11} parameters for both polarizations have minima corresponding to the resonant wavelengths. Similarly, the phase of these parameters, unlike the S_{21} parameters, are close to zero at these wavelengths. From the relative impedance denoted in Fig. 4(c), while the TE and TM exhibit positive real impedance, the imaginary parts are significant and reduce the overall absorbance of the structure even at wavelengths where $Re(Z) \sim 1$.

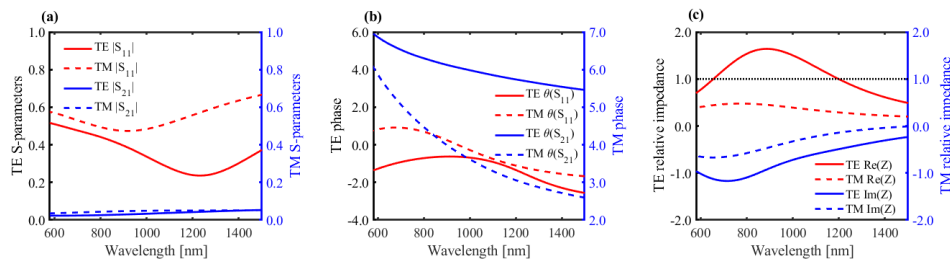


Fig. 4. Calculated (a) S -parameters (b) phase, and (c) relative impedance of the structure for TE and TM polarizations.

3.3. Parametric sweep

Another approach used to distinguish between the different modes in the metamaterial absorbers is how they respond spectrally to the structural parameters. We examine the influence of the period of the top rectangular layer and its width, the thickness of the spacer layer, and the angle of incidence in the rest of the discussion.

Figure 5 shows the influence of the periodicity of the top rectangular structure on the absorbance for both polarizations, (a) TE and (b) TM. Figure 5(c) shows the unpolarized absorbance for selected periods in the spectral region of the spectrometer that was used for the measurements. In Fig. 5(a) and (b), absorption red-shifts in the UV region and decreases in the NIR region with an increasing period for both TE and TM. The resonance shift in the UV region illustrates the additional momentum induced by the rectangular patterned top layer which couples with the incident field at different polarization states of the incident light. However, at higher periods that exceed the sub-wavelength parameters of the WBMA, we identified relatively constant resonances due to the multiply diffraction losses in the proposed structure. Moreover, the broad spectral range from Vis-NIR region is seen to have a minimal reflected field at periods ≤ 300 nm and decreases monotonically by increasing periodicity. Figure 5(c) compares the simulation (Sim) with the experiment (Exp) for the unpolarized case at selected periods 250, 350, and 500 nm, respectively. We identified a shift of the spectral resonances at the Vis-NIR spectral regions and a decrease in absorbance as a function of period.

The influence of the width of the top rectangle on the spectral absorbance is shown in Fig. 6, (a) and (b), for the two polarizations. It is evident that the broad LSP bands for both TE and TM show strong dependence, red-shifting significantly with increasing width of the structure. The narrow PSP band, on the other hand, is insensitive to the variation in the widths. Moreover, as the width approaches the length of the rectangle namely $W > 150$ nm, both the TE and TM exhibit similar absorption due to the fact the structure becomes symmetric, inducing similar

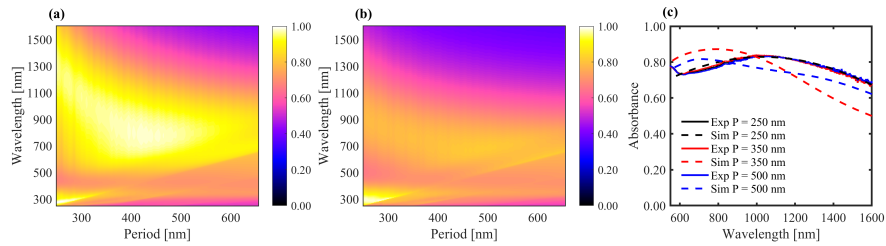


Fig. 5. Spectral absorbance of the MA structure for different periods: (a) TE (b) TM, and (c) extracted absorbance at discrete periods for simulation (Sim) and experiment (Exp) for unpolarized incident light.

charge displacement by the incident field in both polarizations, leading to the similarities in the response. Figure 6(c) compares the simulation results with the experiment for the unpolarized case. In particular, in both cases, whilst the simulation results slightly deviate from that of the experiment, the results confirm that the broad LSP band shows a significant red-shift as the width of the rectangle is increased from 100 to 190 nm. The deviation between both results, as has been pointed out previously and seen in Fig. 1, is attributed to fabrication errors, for example, the deviation of the fabricated top-layer from a perfect rectangle.

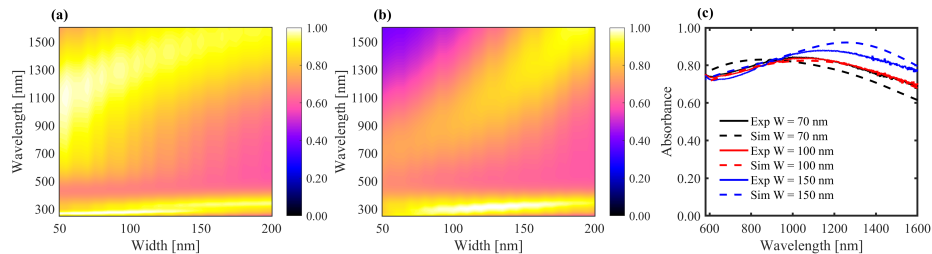


Fig. 6. Spectral absorbance of the structure for different nano-patterned top-layer widths: (a) TE, (b) TM, and (c) extracted absorbance for simulation and experiment at discrete widths for the unpolarized case.

3.4. Polarization properties

As previously indicated, the spacer or dielectric layer plays an important role in the conservation of energy [24,28]. Figure 7 examines the influence of the spacer thickness on the absorbance of the structure. As in all previous cases, the identified peaks in the two polarizations exhibit a different response to the variation of the spacer thickness in some respect. Nevertheless, both the LSP and peaks of the two polarizations exhibit red-shift with increasing spacer thickness [27,28].

For the peak at 280 nm, in a closer examination, while the PSP shows a fair dependence and broadening on the spacer variation in both cases, the TM exhibit a much higher increased in absorbance than the TE.

On the other hand, the LSP of the TM shows a continuous decrease in the absorbance whereas that of the TE increases and then decreases with increasing spacer thickness. From interference theory, the increase in the absorbance arises from the interaction of waves, at the detection plane, returning from the bottom Ti mirror and the top Ti structure leading to either constructive interference of the two waves when the phase-matching condition is achieved or vice versa [28]. Thus, in the case of the TE, the destructive interference of the two waves exists for a much broader spacer thickness than that of the TM, hence, the associated increase in absorbance. Similarly,

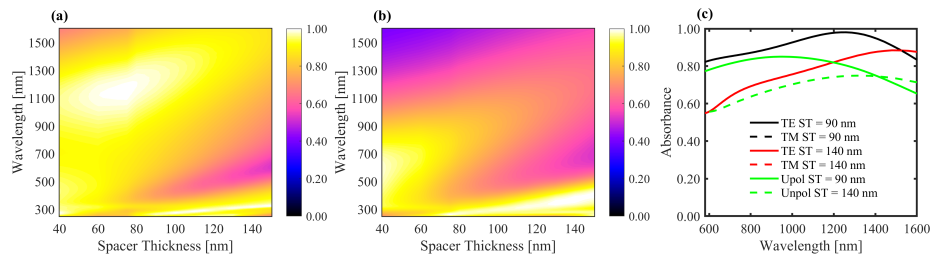


Fig. 7. Spectral absorbance of the MA structure for different spacer thickness: (a) TE (b) TM, and (c) extracted absorbance at discrete spacer thicknesses for polarizations.

the impedance theory [30] suggests that the matching of the free space impedance to that of the structure is satisfied at different thicknesses of the spacer region. Lastly, the spacer thickness significantly affects the LSP band more than the PSP as one would expect [24,27].

3.5. Angle of incidence

For the completeness of metamaterial absorber analyses, one typically considers the angular dependence of the proposed structure. Figure 8(a) and (b) show the simulated angular dependence of our simple structure. Figure 8(c) shows a similar results at discrete polarization angles for both polarizations.

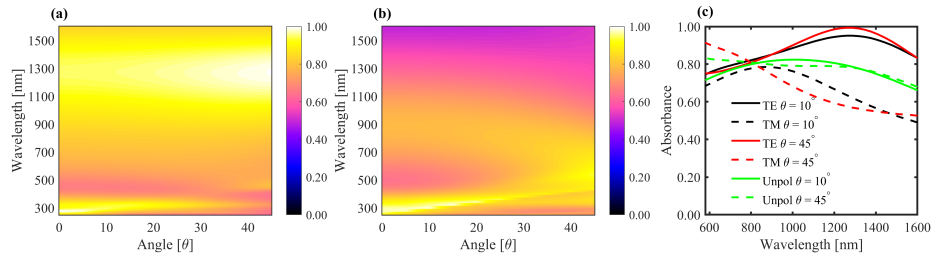


Fig. 8. Spectral absorbance of the MA structure for different angles of incidence: (a) TE (b) TM, and (c) extracted absorbance at discrete angles for both polarizations.

The two polarizations exhibit different angular dependence on two figures. While the two peaks (280 nm and 1350 nm) in the TE demonstrate an almost constant absorption over the chosen angular range, the peaks in the TM case, on the other hand, show a relatively strong angular dependence with decreasing absorption at higher angles. In particular, at an angle of incidence $\theta > \sim 35^\circ$, the PSP band shows a slight redshift whereas the LSP shows a blueshift for the TM polarization. Obviously, the polarization dependence angular response from the structure emanates from its asymmetric nature leading to the induction of different charge distributions for the two polarizations [31]. In the unpolarized case, however, the angular dependence vanishes as shown for $\theta = 10^\circ$ and $\theta = 45^\circ$ in Fig. 8(c).

4. Conclusion

Metamaterials play important role in micro- and nanophotonics for a variety of applications due to the flexibility it brings in controlling optical properties. An example is the absolute control of absorption using metamaterial absorbers, which are ideal for applications such as sensing. Due to the need for absorption over a broad spectral range such as required in solar thermal and single detectors over a wide range, many complicated structures have been proposed. Here, we have

demonstrated that there is still room for simple MIM structures to achieve high absorption from UV to NIR spectral range. Moreover, the proposed structure, unlike other complex metamaterial absorbers, is very easy to fabricate with the traditional lift-off process.

Funding. Academy of Finland (320165, 320166).

Acknowledgements. This work is part of the Academy of Finland Flagship Programme, Photonics Research and Innovation (PREIN), decisions 320165 and 320166. I.I acknowledges Optica for the Optica Foundation Amplify Scholarship. B.O.A. also acknowledges Henri Pesonen for the provision of FMM codes to verify our initial results. B.O.A. and I.I further acknowledges the SPIE for the Optics and Photonics scholarship.

Disclosures. The authors declare that there are no conflicts of interest related to this article.

Data Availability. Data underlying the results presented in this paper are not publicly available at this time but may be obtained from the corresponding authors upon reasonable request.

Supplemental document. See [Supplement 1](#) for supporting content.

References

1. S. Luo, J. Zhao, D. Zuo, and X. Wang, "Perfect narrow band absorber for sensing applications," *Opt. Express* **24**(9), 9288–9294 (2016).
2. L. Shi, Q. Tang, Z. Liu, Y. Liu, Y. Li, G. Liu, and L. Li, "Tunable dual-band plasmonic perfect absorber and its sensing applications," *J. Opt. Soc. Am. B* **36**(10), 2750–2756 (2019).
3. Y. Xu, P. Bai, X. Zhou, Y. Akimov, C. E. Png, L.-K. Ang, W. Knoll, and L. Wu, "Optical refractive index sensors with plasmonic and photonic structures: Promising and inconvenient truth," *Adv. Opt. Mater.* **7**(9), 1801433 (2019).
4. H. A. Atwater and A. Polman, "Plasmonics for improved photovoltaic devices," *Nat. Mater.* **9**(3), 205–213 (2010).
5. V.-C. Su, C. H. Chu, G. Sun, and D. P. Tsai, "Advances in optical metasurfaces: fabrication and applications [invited]," *Opt. Express* **26**(10), 13148–13182 (2018).
6. I. Issah, T. Pihlava, A. R. Rashed, and H. Caglayan, "Mechanism of emitters coupled with a polymer-based hyperbolic metamaterial," *Opt. Express* **30**(6), 8723–8733 (2022).
7. S. A. Maier, *Plasmonics: Fundamentals and Applications* (Springer, New York, 2007).
8. Y. Cui, Y. He, Y. Jin, F. Ding, L. Yang, Y. Ye, S. Zhong, Y. Lin, and S. He, "Plasmonic and metamaterial structures as electromagnetic absorbers," *Laser Photonics Rev.* **8**(4), 495–520 (2014).
9. P. Wu, C. Zhang, Y. Tang, B. Liu, and L. Lv, "A perfect absorber based on similar fabry-perot four-band in the visible range," *Nanomaterials* **10**(3), 488 (2020).
10. Y. Zhu, T. Lan, P. Liu, and J. Yang, "Broadband near-infrared tio2 dielectric metamaterial absorbers," *Appl. Opt.* **58**(26), 7134–7138 (2019).
11. W. Wang, Y. Cui, Y. He, Y. Hao, Y. Lin, X. Tian, T. Ji, and S. He, "Efficient multiband absorber based on one-dimensional periodic metal–dielectric photonic crystal with a reflective substrate," *Opt. Lett.* **39**(2), 331–334 (2014).
12. R. Ma, D. Wu, Y. Liu, H. Ye, and D. Sutherland, "Copper plasmonic metamaterial glazing for directional thermal energy management," *Mater. Des.* **188**, 108407 (2020).
13. J. Piotrowski and A. Rogalski, "Uncooled long wavelength infrared photon detectors," *Infrared Phys. Technol.* **46**(1-2), 115–131 (2004).
14. R. Feng, J. Qiu, L. Liu, W. Ding, and L. Chen, "Parallel lc circuit model for multi-band absorption and preliminary design of radiative cooling," *Opt. Express* **22**(S7), A1713–A1724 (2014).
15. Q. Li, J. Gao, H. Yang, H. Liu, X. Wang, Z. Li, and X. Guo, "Tunable plasmonic absorber based on propagating and localized surface plasmons using metal-dielectric-metal structure," *Plasmonics* **12**(4), 1037–1043 (2017).
16. H. Xu, L. Hu, Y. Lu, J. Xu, and Y. Chen, "Dual-Band Metamaterial Absorbers in the Visible and Near-Infrared Regions," *J. Phys. Chem. C* **123**(15), 10028–10033 (2019).
17. X. Wang, T. Sang, G. Li, Q. Mi, Y. Pei, and Y. Wang, "Ultrabroadband and ultrathin absorber based on an encapsulated t-shaped metasurface," *Opt. Express* **29**(20), 31311–31323 (2021).
18. L. Zhu, Y. Jin, H. Liu, and Y. Liu, "Ultra-broadband absorber based on metal-insulator-metal four-headed arrow nanostructure," *Plasmonics* **15**(6), 2153–2159 (2020).
19. T. S. Tuan and N. T. Q. Hoa, "Numerical study of an efficient broadband metamaterial absorber in visible light region," *IEEE Photonics J.* **11**(3), 1–10 (2019).
20. P. T. Dang, T. V. Vu, J. Kim, J. Park, V.-C. Nguyen, D. D. Vo, T. K. Nguyen, K. Q. Le, and J.-H. Lee, "Efficient broadband truncated-pyramid-based metamaterial absorber in the visible and near-infrared regions," *Crystals* **10**(9), 784 (2020).
21. J. Liu, W.-Z. Ma, W. Chen, G.-X. Yu, Y.-S. Chen, X.-C. Deng, and C.-F. Yang, "Numerical analysis of an ultra-wideband metamaterial absorber with high absorptivity from visible light to near-infrared," *Opt. Express* **28**(16), 23748–23760 (2020).
22. D. Wu, C. Liu, Y. Liu, L. Yu, Z. Yu, L. Chen, R. Ma, and H. Ye, "Numerical study of an ultra-broadband near-perfect solar absorber in the visible and near-infrared region," *Opt. Lett.* **42**(3), 450–453 (2017).

23. M. Lobet, M. Lard, M. Sarrazin, O. Deparis, and L. Henrard, "Plasmon hybridization in pyramidal metamaterials: a route towards ultra-broadband absorption," *Opt. Express* **22**(10), 12678–12690 (2014).
24. Y. Zhou, Z. Qin, Z. Liang, D. Meng, H. Xu, D. R. Smith, and Y. Liu, "Ultra-broadband metamaterial absorbers from long to very long infrared regime," *Light: Sci. Appl.* **10**(1), 138 (2021).
25. F. Ding, J. Dai, Y. Chen, J. Zhu, Y. Jin, and S. I. Bozhevolnyi, "Broadband near-infrared metamaterial absorbers utilizing highly lossy metals," *Sci. Rep.* **6**(1), 39445 (2016).
26. L. Skowronski, "Optical properties of titanium in the regime of the limited light penetration," *Materials* **13**(4), 952 (2020).
27. I. Issah, F. Li, M. Baah, I. A. Otoo, L. Asilevi, P. Bawuah, and B. O. Asamoah, "Passive tunable and polarization-insensitive fan-like metamaterial absorber in the visible spectrum," *J. Opt. Soc. Am. B* **38**(9), C1–C10 (2021).
28. H.-T. Chen, "Interference theory of metamaterial perfect absorbers," *Opt. Express* **20**(7), 7165–7172 (2012).
29. D. R. Smith, S. Schultz, P. Markoš, and C. M. Soukoulis, "Determination of effective permittivity and permeability of metamaterials from reflection and transmission coefficients," *Phys. Rev. B* **65**(19), 195104 (2002).
30. N. I. Landy, S. Sajuyigbe, J. J. Mock, D. R. Smith, and W. J. Padilla, "Perfect metamaterial absorber," *Phys. Rev. Lett.* **100**(20), 207402 (2008).
31. S. Ogawa and M. Kimata, "Metal-insulator-metal-based plasmonic metamaterial absorbers at visible and infrared wavelengths: A review," *Materials* **11**(3), 458 (2018).